International Forum on Aeroelasticity and Structural Dynamics
IFASD 2026
17-21 June 2026, Goettingen, Germany

NUMERICAL VALIDATION OF A HIGH-ASPECT RATIO WING FLEXIBLE AIRCRAFT MODELLED IN AN ENHANCED LOW-FIDELITY FRAMEWORK

Willi Mickein[1], Ralf A. Senger Franco[1], Álvaro A. G. Quesada[1], Pedro J. Gonzalez[1], Flavio J. Silvestre[1], Kilian Streitenberger[2], Wolf-Reiner Krüger[2]

[1]Technical University of Berlin
Straße des 17. Juni 135, 10623 Berlin, Germany
w.mickein@tu-berlin.de
r.sengerfranco@tu-berlin.de
garcia.quesada@tu-berlin.de
p.gonzalez.ramirez@tu-berlin.de
flavio.silvestre@tu-berlin.de

[2]German Aerospace Center
Bunsenstraße 10, 37073 Göttingen, Germany
kilian.streitenberger@dlr.de
wolf.krueger@dlr.de

Keywords: flexible aircraft dynamics, transonic aerodynamics, CFD-based corrections, aeroelasticity

Abstract: The aviation industry has been continuously seeking forms to enhance the aircraft's aerodynamic efficiency, thereby reducing its environmental impact. One focus has been reducing the aircraft's weight while maximizing its lift-to-drag ratio by applying slender elongated wings, the so-called High-Aspect-Ratio (HAR) wings. These lightweight HAR wings introduce substantial structural flexibility to the vehicle, which in turn may cause a problematic coupling between aeroelasticity and flight dynamics. Predicting these phenomena is even more challenging when flying in the transonic regime. The integration of Computational Fluid Dynamics (CFD) and Computational Structural Dynamics (CSD) formulations allows the characterization of phenomena occurring in this regime. However, despite recent advances in computational performance, modern CFD/CSD solvers still require massive simulation time and are therefore unsuitable for many tasks, such as flight and aeroelastic control law design and verification. To address this problem, low fidelity frameworks for the simulation of the flexible aircraft dynamics have been proposed, which offer high computational performance while resembling higher complexity models well enough so that control design, testing and flying quality analyzes are possible. However, the consideration of transonic effects is still a problem in these low-fidelity models. In this work, a CFD-based correction form for transonic effects in a low-fidelity model of the flexible aircraft dynamics using strip theory is studied. The derived model is numerically validated for the DLR-F25 virtual reference aircraft through a comparative analysis of its longitudinal behavior against CFD data in the time and frequency domain. The results show a good qualitative and quantitative agreement of the rigid body and flexible flight dynamics in both domains. They therefore reinforce the proposed framework's ability to capture complex transonic aeroelastic effects with high computational efficiency.

1 INTRODUCTION

The field of aerospace engineering is continuously searching for ways to enhance aerodynamic efficiency and to reduce environmental impact. One of the current areas of interest is the development and research of lighter and more aerodynamically efficient wings. This has led to the design of slender wing structures, so called High-Aspect-Ratio (HAR) wings. As a consequence of this design approach, these wings exhibit increased flexibility and may therefore experience higher deformation during flight. This inherent flexibility also leads to a reduction of the frequency of the elastic modes down to the region of the faster aircraft dynamics modes. Thus, HAR-wing aircraft can show a tendency for a relevant coupling between flight dynamics and aeroelastic modes, which is accompanied by significant challenges when developing control laws for flexible airplanes [1–3]. As such, the integration of aeroelastic dynamics into the flight dynamic models is mandatory to properly represent the dynamics of HAR airplanes. This can be achieved using a variety of approaches. One significant difference between them is whether the modal superposition principle, proposed by Waszak and Schmidt in 1988 [4], is used to describe the dynamics of the structure, which is therefore considered (geometrically) linear. Different examples that use this principle are: VarLoads (DLR), Loads Kernel (DLR), ModSiG (TU-Berlin), ITA-STAR (Aeronautical Institute of Technology-ITA) and G-Flights (TU-Hamburg) [5–9]. Some codes and toolboxes that do not use this principle and rely on a geometrically non-linear formulation, are UM/NAST (The University of Michigan's Nonlinear Aeroelastic Simulation Toolbox), SHARPy (Imperial College), Aeroflex (Aeronautical Institute of Technology-ITA), NBS-Nonlinear Beam Shape (University of Bristol) and Modal Rotation Method Formulation (Technion) [10–14]. Another differentiation comes from the aerodynamic modeling, where, for example, quasi-steady/unsteady strip theory, vortex/doublet lattice methods, or computational fluid dynamics (CFD) formulations can be implemented. In the simulation under transonic flight conditions, CFD and Computational Structural Dynamics methodologies are widely used, since they allow for the characterization of phenomena like shock formation and unsteady buffet effects, in their full complexity. Thanks to the recent advances in computational performance, these toolboxes/frameworks can be used in highly sophisticated simulation models that closely resemble their real-world counterparts. However, the massive simulation time (hours to days) associated with these processes makes them unsuitable for preliminary design, multi-disciplinary optimization, flight and aeroelastic control law design and real-time applications involving flexible aircraft. To address this problem, the TU Berlin - ModSiG (Modeling and Simulation Group) has created a numerical low-fidelity framework for the simulation of flexible aircraft. The coupled aircraft dynamics is written on the basis of linearized mean axes constraints [4] and the principle of modal superposition is applied. An unsteady strip theory formulation in the time domain is used to calculate the incremental aerodynamic forces and moments [7]. This work describes the methodology behind the ModSiG framework and the modification of the low-fidelity unsteady strip theory with data derived from higher-fidelity CFD simulations to sufficiently account for transonic dynamics. The derived non-linear model is numerically validated for the DLR-F25 virtual reference aircraft [15] through a comparative analysis of its longitudinal behavior against full CFD data, obtained from CFD simulations with UltraFLoads [16], in the time and frequency domain. A use case of the validated model is presented in [17], where a straightforward active longitudinal load control methodology for a HAR aircraft is derived.

2 DEVELOPMENT OF A LOW-ORDER FLIGHT SIMULATION MODEL FOR A HIGH-ASPECT RATIO WING AIRCRAFT

The following subsections will briefly present the formulations, which enable the derivation of the model of a free-flying flexible aircraft. The modeling process, depicted in Fig. 1, involves the ModSiG (Modeling and Simulation Group) framework [7].

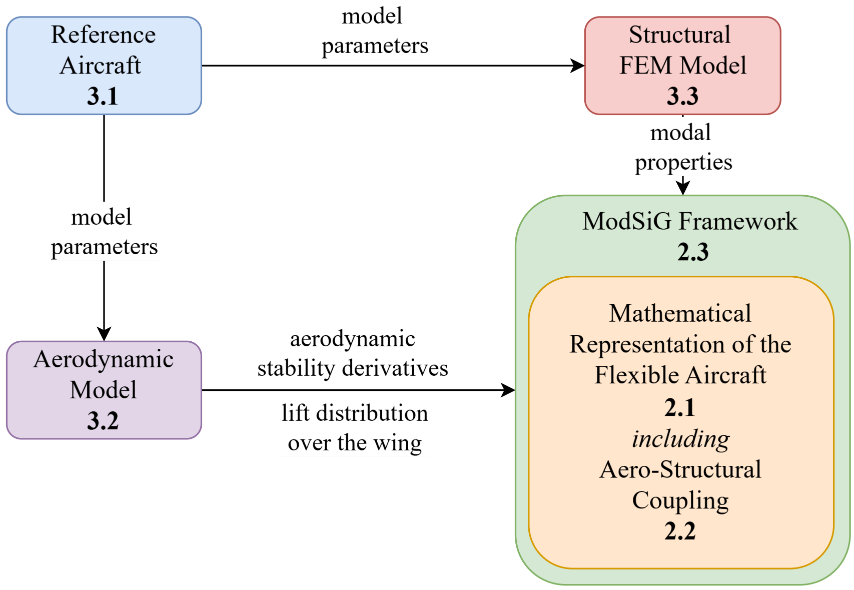

Figure 1: Workflow for generating the model of a flexible aircraft with the ModSiG framework

2.1 Mathematical Representation of the Flexible Aircraft

The baseline of the mathematical representation of the aircraft in the framework are the (non-linear) equations of motion based on the mean axes formulation [4], the unsteady incremental aerodynamics modeling via strip theory with three-dimensional corrections [18] and the quasi-steady incremental aerodynamics modeling technique from [4] and [19]. The methodology can be applied under the following assumptions:

- Flexible aircraft with small elastic displacements compared to the aircraft geometry, so that the structural dynamics can be assumed to be linear.
- High-aspect ratio aircraft, for which the two-dimensional aerodynamic strip theory represents a good approximation.
- Operation in an incompressible flow regime.

The modal superposition technique is used to represent the aircraft's structural dynamics [4, 19, 20]. It transforms a model in such a way that it is no longer represented by 6-degree-of-freedom elements but, additionally, by its modal eigenmodes. Thus, the aircraft deformation $\mathbf{p_d}$ can be described in the global body reference frame (GBRF) by the following equation:

$$\mathbf{p_d}_{\mathrm{B(G)}} = \mathbf{\Phi}(x, y, z)\eta(t) \tag{1}$$

where $\mathbf{\Phi}_{\mathbf{n_e}\times\mathbf{1}}$ is the modal matrix, n_e is the number of elastic modes of the free-body undamped vibration problem and $\eta_{\mathbf{n_e}\times\mathbf{1}}$ is the vector of the modal amplitudes. Based on this, the following vector equations are used to represent the flexible aircraft mathematically [21]:

$$\dot{\mathbf{V}}_{\mathrm{B(G)}}(t) = -\boldsymbol{\omega}_{\mathrm{B(G)}}(t) \times \mathbf{V}_{\mathrm{B(G)}}(t) + \mathbf{T}_{\mathrm{B(G)I}}(t)\mathbf{G_I} + \frac{1}{m}\mathbf{F}^{\mathrm{ext}}_{\mathrm{B(G)}}(t) \tag{2}$$

$$\dot{\boldsymbol{\omega}}_{\mathrm{B(G)}}(t) = -\mathbf{J}^{-1}\left(\boldsymbol{\omega}_{\mathrm{B(G)}}(t) \times (\mathbf{J}\boldsymbol{\omega}_{\mathrm{B(G)}}(t))\right) + \mathbf{J^{-1}}\mathbf{M}^{\mathrm{ext}}_{\mathrm{B(G)}}(t) \tag{3}$$

$$\ddot{\eta}_k\,(t) = -2\xi_k\omega_{n_k}\dot{\eta}_k(t) - \omega^2_{n_k}\eta_k(t) + \mu_k^{-1}Q_{\eta_k}(t), \quad \text{for } k = 1, 2, ..., n_e. \tag{4}$$

The first two represent the differential equations of the classic rigid body flight dynamics. Wherein $\dot{\mathbf{V}}_{\mathrm{B(G)}}$ and $\boldsymbol{\omega}_{\mathrm{B(G)}}$ are the linear and angular velocities, respectively, written in the GBRF; $\mathbf{T}_{\mathrm{B(G)I}}$ is the transformation matrix from the inertial reference frame to the GBRF; $\mathbf{J}$ is the inertia tensor; and $\mathbf{F}^{\mathrm{ext}}_{\mathrm{B(G)}}$ and $\mathrm{M}^{\mathrm{ext}}_{\mathrm{B(G)}}$ are, respectively, the external forces and moments written in the GBRF. Earth gravity is considered by the vector $\mathbf{G_I}$.
The third equation describes the aeroelastic dynamics in modal coordinates; see also [18]. Here η_k is the amplitude of the k-th elastic modal shape, ξ_k is the structural damping of the k-th elastic mode and ω_{n_k} is the *in vacuum* natural frequency, μ_k is the corresponding entry of the k-th elastic mode in the matrix μ and n_e is the number of elastic modes of interest. The modal mass matrix μ is a diagonal matrix defined as follows:

$$\mu = \mathbf{\Lambda^T M \Lambda} \tag{5}$$

Here $\mathbf{M}$ is the mass matrix and $\mathbf{\Lambda}$ is the matrix of eigenvectors of the structural dynamics problems. The system's physical coordinates are collected in the vector $\mathbf{q}$ as follows.

$$\mathbf{q}(t) = \mathbf{\Lambda}\eta(t) \tag{6}$$

The aerodynamic forces $\mathbf{F}^{\mathrm{ext}}_{\mathrm{B(G)}}$ and moments $\mathrm{M}^{\mathrm{ext}}_{\mathrm{B(G)}}$ and aerodynamic generalized loads Q_η can be computed within the ModSiG-FMRA framework using different approaches (unsteady aerodynamics, quasi-steady aerodynamics, with or without follower forces and local stall effects). Incremental aerodynamics in incompressible flow due to elastic deformations are modeled in the time domain, applying strip theory at different complexity levels [7]. According to strip theory, the surface producing lift is divided into a finite number of elements or panels that are treated independently. The lifting surfaces (wing, horizontal and vertical empennage) are assumed to have thin profiles and structural linear vertical displacements (along the z-axis of the mean axes reference frame) are considered, but chordwise deformation is neglected. The lifting surfaces of the structural aircraft model have been reduced to beams by means of Guyan reduction [22], which allows to directly interpolate the beam structural points to the aerodynamic center position per aerodynamic strip.
As a result of the enforcement of the linearized mean axes constraints, the equations of the structural dynamics and the equations of the flight dynamics are inertially decoupled. This assumption applies up to moderate deformations [23]. The considered coupling arises due to the external forces $\mathbf{F}^{\mathrm{ext}}_{\mathrm{B(G)}}$ and moments $\mathrm{M}^{\mathrm{ext}}_{\mathrm{B(G)}}$, which are influenced by the rigid body states and the deformations, and the incremental generalized forces Q, which are influenced by the rigid body states as well as the mode shapes. This is described in more detail in the following subsection 2.2.

2.2 Aero-Structural Coupling

The coupling between the rigid body dynamics (Eq. 2 and Eq. 3) and the structural dynamics (Eq. 4) is present due to the external aerodynamic forces and moments, which consist of both rigid body and flexible contributions. In mathematical notation, the incremental component due to deformation can be expressed as in [18]:

$$
\begin{aligned}
\mathbf{F}^{\text{aero}}_{\text{B(G)}} &= \mathbf{F}^{\text{aero (NC)}}_{\text{B(G)}}(t) + \mathbf{F}^{\text{aero (C)}}_{\text{B(G)}}(t) \\
&= \rho(t)\,\mathbf{F}^{\text{aero (NC)}}_{\ddot{\eta}}(t)\,\ddot{\boldsymbol{\eta}}(t) \\
&+ \rho(t)\,V(t)\,\mathbf{F}^{\text{aero (NC)}}_{\dot{\eta}}(t)\,\dot{\boldsymbol{\eta}}(t) + \rho(t)\,V(t)\,\mathbf{F}^{\text{aero (C)}}_{\dot{\eta}}(t)\,\dot{\boldsymbol{\eta}}(t) \\
&+\ \rho(t)\,V^2(t)\,\mathbf{F}^{\text{aero (NC)}}_{\eta}(t)\,\boldsymbol{\eta}(t) \\
&+\ \rho(t)\,V(t)\,\mathbf{F}^{\text{aero (NC)}}_{\lambda}(t)\left(\boldsymbol{\lambda_1}(t) + \boldsymbol{\lambda_2}(t)\right)
\end{aligned} \tag{7}
$$

$$
\begin{aligned}
\mathbf{M}^{\text{aero}}_{\text{B(G)}} &= \mathbf{M}^{\text{aero (NC)}}_{\text{B(G)}}(t) + \mathbf{M}^{\text{aero (C)}}_{\text{B(G)}}(t) \\
&= \rho(t)\,\mathbf{M}^{\text{aero (NC)}}_{\ddot{\eta}}(t)\,\ddot{\boldsymbol{\eta}}(t) \\
&+ \rho(t)\,V(t)\,\mathbf{M}^{\text{aero (NC)}}_{\dot{\eta}}(t)\,\dot{\boldsymbol{\eta}}(t) + \rho(t)\,V(t)\,\mathbf{M}^{\text{aero (C)}}_{\dot{\eta}}(t)\,\dot{\boldsymbol{\eta}}(t) \\
&+ \rho(t)\,V^2(t)\,\mathbf{M}^{\text{aero (NC)}}_{\eta}(t)\,\boldsymbol{\eta}(t) + \rho(t)\,V^2(t)\,\mathbf{M}^{\text{aero (C)}}_{\eta}(t)\,\boldsymbol{\eta}(t) \\
&+\ \rho(t)\,V(t)\,\mathbf{M}^{\text{aero (NC)}}_{\lambda}(t)\left(\boldsymbol{\lambda_1}(t) + \boldsymbol{\lambda_2}(t)\right)
\end{aligned} \tag{8}
$$

The incremental aerodynamic forces and moments with circulatory (C) and non-circulatory (NC) contributions in Eq. 7 and 8 are terms that depend on the spanwise aerodynamic distribution, the geometry and the modal properties. Further details on these dependencies are found in reference [18], where the applied methodology is presented.
The flexible contribution due to incremental aerodynamics is supplemented by the differential equations of each aerodynamic lag state λ, which are defined as two states per strip for each lifting surface. The aerodynamic lag states (λ_{1_i} and λ_{2_i}) describe the unsteady behavior of the airflow for the i-th strip of the lifting surface, which is dependent on the time derivative of the spanwise downwash $\dot{w}^f_{3/4}(t)$, the airspeed V, the modal amplitudes $\eta(t)$, velocities $\dot{\eta}(t)$ and accelerations $\ddot{\eta}(t)$:

$$
\begin{aligned}
\dot{\lambda}_{1_i}(t) &= 2V(t)\,a_1 c^{-1}\lambda_{1_i}(t) + A_1\dot{w}^f_{3/4}(t) \\
\dot{\lambda}_{2_i}(t) &= 2V(t)\,a_2 c^{-1}\lambda_{2_i}(t) + A_2\dot{w}^f_{3/4}(t)
\end{aligned} \tag{9}
$$

The aero-structural coupling is present in Eq. 4 due to the generalized forces Q. They are dependent on $\eta(t)$, $\dot{\eta}(t)$, $\ddot{\eta}(t)$, λ, the aircraft states X_{states}, as well as the control variables $u_{control}$. To emphasize this, Eq. 4 is rewritten as Eq. 10, where Q is split into its components. There, the different $\mathbf{Q}_{\eta_\mathbf{x}}$ are the vectors of the generalized forces depending on x, where x is one of the variables named above. At the top right, a superscript denotes whether the generalized loads are calculated via the quasi-steady approach (QS) [19] or the unsteady approach (C for circulatory contribution or NC for non-circulatory contribution) [18].

$$
\begin{aligned}
\left[\boldsymbol{\mu} - \rho(t)\,\boldsymbol{Q}^{(\text{NC})}_{\eta_{\ddot{\eta}}}(t)\right]\ddot{\boldsymbol{\eta}}(t) &= \left[-2\boldsymbol{\mu}\boldsymbol{\xi}\boldsymbol{\omega_n} + \rho(t)\,V(t)\left(\boldsymbol{Q}^{(\text{NC})}_{\eta_{\dot{\eta}}}(t) + \boldsymbol{Q}^{(C)}_{\eta_{\dot{\eta}}}(t)\right)\right]\dot{\boldsymbol{\eta}}(t) \\
&+ \left[-\boldsymbol{\mu}\boldsymbol{\omega_n^2} + \rho(t)\,V^2(t)\left(\boldsymbol{Q}^{(NC)}_{\eta_\eta}(t) + \boldsymbol{Q}^{(C)}_{\eta_\eta}(t)\right)\right]\boldsymbol{\eta}(t) \\
&+ \rho(t)\,V(t)\,\boldsymbol{Q}^{(C)}_{\eta_\lambda}\left(\boldsymbol{\lambda_1}(t) + \boldsymbol{\lambda_2}(t)\right) \\
&+ \frac{1}{2}\rho(t)\,V^2(t)\,S\bar{c}\boldsymbol{Q}^{(\text{QS})}_{\eta_{X_{state}}}\boldsymbol{X}_{state}(t) \\
&+ \frac{1}{2}\rho(t)\,V^2(t)\,S\bar{c}\boldsymbol{Q}^{(\text{QS})}_{\eta_{u_{control}}}\boldsymbol{u}_{control}(t)
\end{aligned} \tag{10}
$$

The equation above can be converted into a system of first order differential equations:

$$\begin{bmatrix}\dot{\boldsymbol{\eta}}(t)\\ \ddot{\boldsymbol{\eta}}(t)\end{bmatrix} = \begin{bmatrix}\mathbf{0}_{n_e\times n_e} & \boldsymbol{I}_{n_e\times n_e}\\ \boldsymbol{\Pi}_1(t) & \boldsymbol{\Pi}_2(t)\end{bmatrix}\begin{bmatrix}\boldsymbol{\eta}(t)\\ \dot{\boldsymbol{\eta}}(t)\end{bmatrix} + \begin{bmatrix}\mathbf{0}_{n_e\times n_e}\\ \boldsymbol{\Pi}_3(t)\end{bmatrix}(\boldsymbol{\lambda}_1(t)+\boldsymbol{\lambda}_2(t))$$
$$+\begin{bmatrix}\mathbf{0}_{n_e\times n_e}\\ \boldsymbol{\Pi}_4(t)\end{bmatrix}\boldsymbol{X}_{state}(t) + \begin{bmatrix}\mathbf{0}_{n_e\times n_e}\\ \boldsymbol{\Pi}_5(t)\end{bmatrix}\boldsymbol{u}_{control}(t) \tag{11}$$

The matrices $\boldsymbol{\Pi}_1, \boldsymbol{\Pi}_2, \boldsymbol{\Pi}_3, \boldsymbol{\Pi}_4, \boldsymbol{\Pi}_5$ are defined as:

$$\begin{aligned}
\boldsymbol{\Pi}_1(t) &= \left[\boldsymbol{\mu}-\rho(t)\,\boldsymbol{Q}^{(\mathrm{NC})}_{\eta\ddot{\eta}}(t)\right]^{-1}\left[-\boldsymbol{\mu}\omega_n^2+\rho(t)\,V^2(t)\left(\boldsymbol{Q}^{(NC)}_{\eta\dot{\eta}}(t)+\boldsymbol{Q}^{(C)}_{\eta\dot{\eta}}(t)\right)\right]\\
\boldsymbol{\Pi}_2(t) &= \left[\boldsymbol{\mu}-\rho(t)\,\boldsymbol{Q}^{(\mathrm{NC})}_{\eta\ddot{\eta}}(t)\right]^{-1}\left[-2\boldsymbol{\mu}\boldsymbol{\xi}\omega_n+\rho(t)\,V(t)\left(\boldsymbol{Q}^{(NC)}_{\eta\dot{\eta}}(t)+\boldsymbol{Q}^{(C)}_{\eta\dot{\eta}}(t)\right)\right]\\
\boldsymbol{\Pi}_3(t) &= \left[\boldsymbol{\mu}-\rho(t)\,\boldsymbol{Q}^{(\mathrm{NC})}_{\eta\ddot{\eta}}(t)\right]^{-1}\rho(t)\,V(t)\,\boldsymbol{Q}^{(C)}_{\eta\lambda}(t)\\
\boldsymbol{\Pi}_4(t) &= \left[\boldsymbol{\mu}-\rho(t)\,\boldsymbol{Q}^{(\mathrm{NC})}_{\eta\ddot{\eta}}(t)\right]^{-1}\frac{1}{2}\rho(t)\,V^2(t)\,S\bar{c}\boldsymbol{Q}^{(\mathrm{QS})}_{\eta X_{state}}(t)\\
\boldsymbol{\Pi}_5(t) &= \left[\boldsymbol{\mu}-\rho(t)\,\boldsymbol{Q}^{(\mathrm{NC})}_{\eta\ddot{\eta}}(t)\right]^{-1}\frac{1}{2}\rho(t)\,V^2(t)\,S\bar{c}\boldsymbol{Q}^{(\mathrm{QS})}_{\eta u_{control}}(t)
\end{aligned} \tag{12}$$

2.3 ModSiG-FMRA Framework

In Fig. 2 the workflow of the numerical framework ModSiG-FMRA is represented.

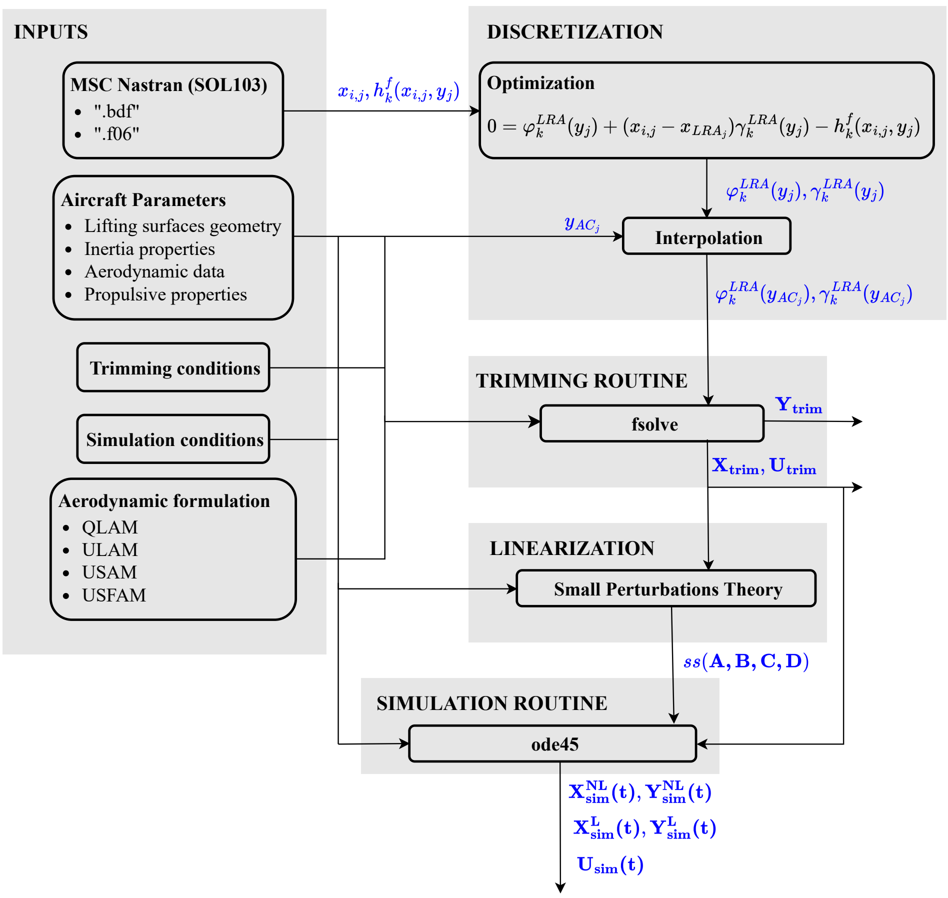

Figure 2: Workflow of the ModSiG Framework [7]

The usage of the modal superposition technique for representing the aircraft's structural dynamics requires the definition of the aircraft modal basis as input of the framework [7]. The modal analysis of the corresponding aircraft model is carried out in MSC Nastran with SOL103. The output file ".f06" contains the undamped natural frequencies $\omega_{n,k}$ and inertia parameters. Also included are the translational component in the z-direction ($\varphi_k^{LRA}(y_j)$) and the rotational component around the y-axis ($\gamma_k^{LRA}(y_j)$) of the eigenvectors of the structural nodes in the load reference axes (LRA). The subscripts k and j denote here the elastic mode and the corresponding structural node respectively. The SOL103 output file ".bdf" provides the position of the structural nodes as additional input for the framework, if structural discretization is necessary. The usage of strip theory to model the aircraft aerodynamics makes it necessary to use the distributed aerodynamics of the lift and control surfaces as input for the framework. From this distribution, the modal basis of the LRA ($\varphi_k^{LRA}(y_j)$ and $\gamma_k^{LRA}(y_j)$) according to the structural nodes positions is interpolated at the aerodynamic centers y_{AC}. Thus, $\varphi_k^{LRA}(y_{AC_j})$ and $\gamma_k^{LRA}(y_{AC_j})$ are obtained. The propulsive properties, such as engine thrust functions, angular attitude and position have to be predefined. The general geometric parameters of the lifting surfaces, such as span, chord distribution and surface areas, are defined as framework inputs. After defining the trim and simulation conditions, the numerical trimming routine can be performed in Matlab. Using the theory of small perturbations, the state-space matrices of the system (A, B, C, D) are obtained. Lastly, the framework provides a way to simulate the non-linear and the linear system in Simulink and to collect the desired data.

3 TESTCASE DLR-F25

The capabilities of the process outlined above are demonstrated by deriving and numerically validating a non-linear model of a cruise configuration of the DLR-F25 used in the research project Ultra Performance Wing (UP Wing). This project investigates the usage of a HAR wing to increase aerodynamic efficiency and targets a fuel burn reduction of up to $30\,\%$ compared to a state-of-the-art aircraft [24]. To validate that this model represents the aircraft dynamics of a higher complexity model in longitudinal motion, a comparative study is conducted and the results are shown and discussed in section 4.

3.1 Reference Aircraft DLR-F25

Within the federal aviation research program VirEnfREI [25] the DLR-F25 [15], a HAR flexible aircraft, has been developed. It represents a typical commercial aircraft configuration for the short to medium range and a version thereof is considered as the reference aircraft in this work. Table 1 shows the global properties of this DLR-F25 version [26]: While the first two

Table 1: Global properties of the UP Wing model DLR-F25 cruise configuration (MCRUI)

Global Properties	
Wing span	$45\,\mathrm{m}$
Wing area	$130.1\,\mathrm{m}^2$
Aspect ratio	15.6
Cruise mass	$81018.49\,\mathrm{kg}$
Cruise mach number	0.78
Initial cruise altitude	$10258\,\mathrm{m}$

assumptions regarding the methodology used to derive the non-linear ModSiG model based on unsteady aerodynamics listed at the beginning of section 2.1 (moderate deformations and high aspect-ratio aircraft) are applicable here, the same cannot be said for the third assumption (operation in incompressible flow regime). Therefore, three different measures are applied during the modeling process to take into account the transonic cruise condition. Firstly, during the aerodynamic calculations of the flight dynamics coefficients with AVL (see 3.2), the Prandtl-Glauert compressibility correction is used. Secondly, it is not the cruise Mach number (M) that is used for these calculations, but instead the corrected Mach number perpendicular to the quarter chord line of the wing: $M_{corr} = M \cdot cos(\Lambda)$. $\Lambda = 27.4\,^{\circ}$ is the sweep angle of the aircraft. Lastly, for the calculation of the incremental aerodynamics due to flexible deformation, data from CFD computations is additionally used along with the data obtained from Athena Vortex Lattice (AVL) [27], where the aircraft is modeled as a series of bound vortices. This will be discussed in greater detail in the following section.

3.2 Aerodynamic Modeling

To derive a first 6 degree-of-freedom (DoF) flight dynamics model of the flexible aircraft the rigid body model is built within the software AVL and the rigid body stability derivatives are extracted from there in the initial development. Figure 3 shows the developed AVL model. The wing and both nacelles, as well as the horizontal (HTP) and vertical tailplane (VTP) are modeled. The number of panels in span- and chord-wise direction for each element are shown in the following Table 2. The control surface layout is defined in [28], as well as the profiles for each section of the wing.

Table 2: number of panels in the AVL model

	wing	HTP	VTP	nacelle
number of chord-wise panels	30	15	15	6
number of span-wise panels	146	30	20	12

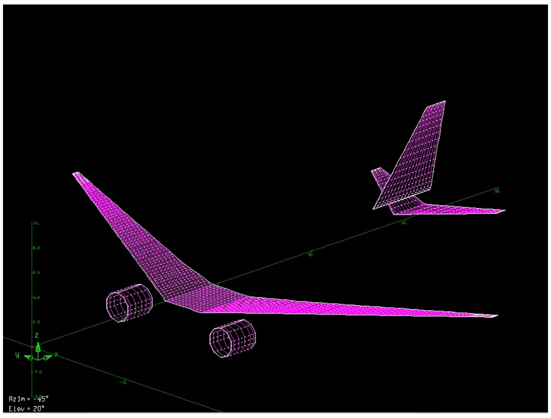

Figure 3: Rigid body AVL model of the UP Wing DLR-F25 baseline [17]

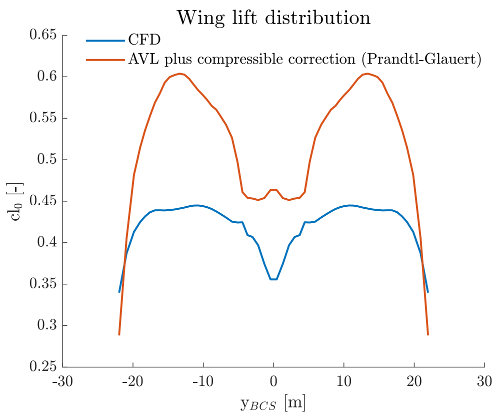

Figure 4: Wing lift distribution for $\alpha = 0°$

To obtain the desired parameters, AVL is used to trim the aircraft in horizontal flight at different angles of attack. From the simulation results, the stability derivatives are then extracted to develop the rigid body flight dynamics model. Figure 4 compares the distributed lift coefficient per unit span, for a zero angle of attack from the CFD simulation [26] and the AVL data. In this regard, the CFD simulation considers the aircraft as a flexible body, whereas AVL represents the aircraft as a rigid body. As shown, the CFD-based transonic distributed aerodynamic behavior over the wing is considerably different from the AVL with compressible correction (Prandtl-Glauert) data for the cruise condition. This cannot be explained by the difference between rigid and flexible models alone. It is also caused by transonic phenomena, which occur in

this operating point and cannot be accurately modeled with AVL. To account for these effects, the distributed aerodynamic slopes C_{L_α} and C_{D_α}, as well as the zero lift and zero drag angle of attack distributions C_{L_0} and C_{D_0} obtained from AVL are exchanged with data from the higher complexity CFD simulations. These slopes and distributions, obtained from CFD data, are used when the incremental aerodynamic coefficients due to flexible deformation are calculated. The principal factors affecting the accuracy of the modeling procedure are the twist and camber distributions defined by the jig shape, as provided with the Finite Element (FE) model. These distributions are captured through the profile coordinates at each wing section and directly affect the computation of the stability derivatives.
For this study, with focus on longitudinal motion, further accuracy between the non-linear ModSiG model and the CFD model is achieved with the correction of the following longitudinal stability derivatives: C_{L_0}, C_{L_α}, C_{L_q}, $C_{L_{\delta_e}}$, C_{m_0}, C_{m_α}, C_{m_q} and $C_{m_{\delta_e}}$. All other derivatives that are obtained from AVL and are necessary to represent the flexible flight dynamics in 6 DoF are maintained.

3.3 Structural Modeling

The structural dynamics of the flexible aircraft are characterized in the modal domain by the modal mass and damping matrices, as formulated in Eq. 10. These modal properties are extracted from the FE model developed and provided by the DLR, depicted in Fig. 5.

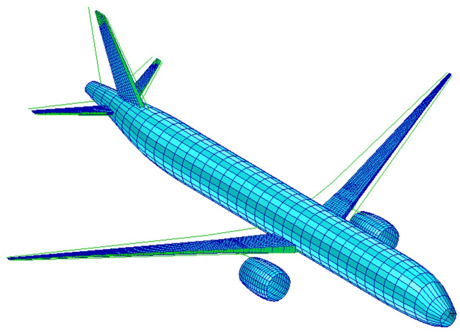

Figure 5: Global FE model of the used DLR-F25 model [25]

In the representation at hand, the FE model includes a load reference axis where the structural properties are condensed, leading to an equivalent beam representation [22]. Since the complete modal properties of the FE model are transferred to the load reference axis, the modal properties are extracted from this condensed representation. The modal analysis provides insights into the flexible behavior of the aircraft and has a direct influence on the modeling process, as shown in the structural dynamics equation. For the derivation of the non-linear ModSiG simulation model, a total of 20 structural modes are considered, covering frequencies up to 15 Hz due to considerations regarding physical reliability and numerical stability. Beyond 15 Hz, the power spectral density of turbulence is already weak, such that the higher frequency modes will not be considerably excited. Therefore, the selection of 20 modes up to 15 Hz ensures a physically reliable and sufficient representation of the flexible aircraft. A brief overview of the first 20 eigenmodes is presented in the Appendix in Table 7.

3.4 CFD Data Acquisition

For the CFD-based aeroelastic simulations of the free flying flexible aircraft, the python-based framework UltraFLoads is used [16]. It is based on the FlowSimulator environmet to utilize the

DLR-TAU Code for solving the unsteady Reynolds-Averaged Navier–Stokes (uRANS) equations with various turbulence models [29–32]. In this paper, the one-equation Spalart-Allmaras turbulence model is used. To accelerate the simulation, the viscous boundary layer is resolved only on the main wing, but not on fuselage, HTP, VTP and engine. This leads to a half model mesh size of approximately 2.4 Mio. grid points, which is shown in Fig. 6.

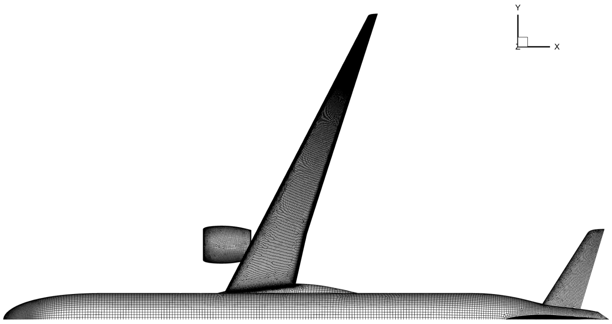

Figure 6: Half model CFD mesh

To incorporate control surface deflections, the mesh-morphing approach of UltraFLoads is used. The model used is capable of using linear structural dynamics, non-linear flight dynamics and aerodynamics, based on uRANS to capture all non-linear aerodynamic effects in the time domain within the transonic regime.

4 COMPARISON OF THE UNSTEADY AERODYNAMICS NON-LINEAR MODSIG MODEL BEHAVIOR TO HIGH-COMPLEXITY CFD SIMULATIONS

4.1 Time Domain Comparison

To compare the time domain response of the non-linear ModSiG model with the data obtained from the high-complexity CFD simulation environment UltraFLoads from the DLR [16], a simulation of an elevator doublet is performed and the longitudinal response of the aircraft is analyzed. The diagrams in Fig. 7 show the input signal (elevator deflection), angle of attack, pitch rate and load factor at the aircraft's center of gravity (CG).

A numerical comparison of the variables mentioned above from both simulations is made in Table 3. Since all variables display oscillating behavior, the absolute values of the oscillation peaks are compared. In addition, the angles of attack of both simulations are compared at the start of the simulation under the trimmed condition. It also includes the absolute and relative differences between the CFD data and the non-linear ModSiG model data.

Table 3: Comparison of longitudinal motion variables: non-linear ModSiG model vs. CFD simulation

	0 s	first peak			second peak			third peak		
	α [°]	$n_z[-]$	$q\left[\frac{\circ}{s}\right]$	α [°]	$n_z[-]$	$q\left[\frac{\circ}{s}\right]$	α [°]	$n_z[-]$	$q\left[\frac{\circ}{s}\right]$	α [°]
CFD	1.32	0.73	-1.51	0.38	1.24	2.23	2.25	0.95	-0.65	1.11
ModSiG	1.34	0.71	-1.68	0.34	1.27	2.44	2.35	0.92	-0.87	1.02
abs. diff. $[-]$	0.02	0.02	0.17	0.04	0.03	0.21	0.1	0.03	0.22	0.09
rel. diff. $[\%]$	1.4	3.02	9.65	12.67	2.5	8.47	4.28	3.09	24.52	8.68

In the trim point, the difference in the angle of attack is very small, with a relative difference of $1.4\,\%$. The agreement in the trimmed conditions of the aircraft between both models is achieved by a thorough modeling procedure in AVL and the application of the aforementioned correction

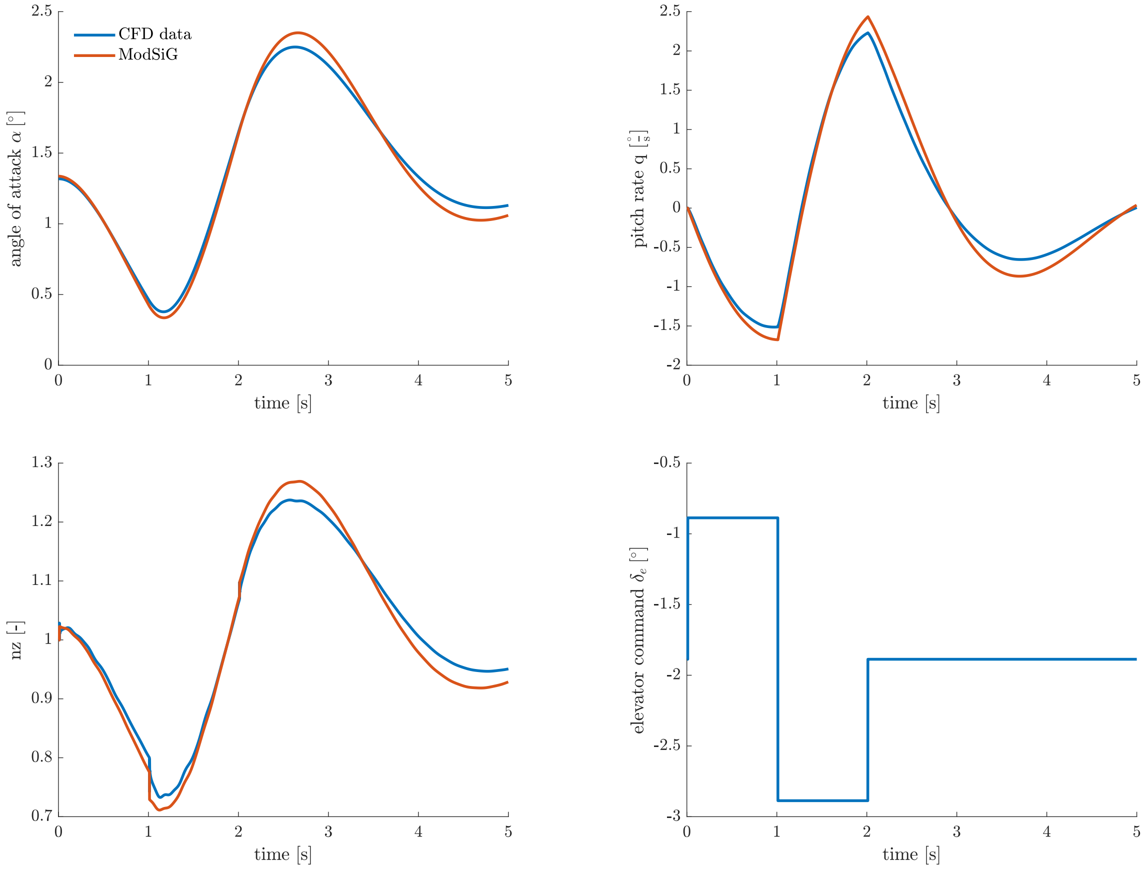

Figure 7: Comparison of the higher fidelity CFD data and the non-linear ModSiG model for a 0.5Hz elevator doublet input

to account for the transonic conditions. The responses of the angle of attack, the pitch rate and the load factor show a very close qualitative match. However, a small difference in the amplitude of the oscillations is visible. The non-linear ModSiG model produces oscillations with larger amplitudes. This is due to the difference in the calculation of the aerodynamic forces on the control surfaces. Since the non-linear ModSiG model utilizes quasi-steady aerodynamics for this, sudden changes in elevator deflection cause immediate changes in the aerodynamic forces. In comparison, in the CFD simulation, which uses unsteady aerodynamics, the aerodynamic forces change only gradually after sudden changes in the deflection of the elevator [18]. A possible further cause for the stated differences is the absence of the fuselage in the AVL model. The fuselage generates a non-negligible part of the lift and pitch moment of the airplane. An adequate representation of this effect in AVL simulations is not trivial, since even with a geometrically correct modeled fuselage further corrections in the calculations are necessary to properly represent the effects that a modeled fuselage causes in CFD simulations. Further comparisons in the time domain are shown in Figures 9, 10 and 11 in the Appendix. There, the acceleration in the z-direction at discrete points on the structure and the pitch rate in the CG due to elevator doublets with different frequencies ($0.5\,$Hz, $3\,$Hz, $10\,$Hz) are shown. Oscillations due to flexibility are present in all simulations. The frequency matches very well and despite differences in amplitude, especially for the accelerations far from the CG (last pax position and cockpit), the trends are captured very well by the corrected model. For the accelerations at the location of the last passenger and the cockpit, the initial acceleration due to the elevator input is stronger in the CFD simulation; however, for the wingtip, the reverse is true. After the initial differences, a convergence of the amplitudes is visible. However, while they are consistently larger in the CFD data for the cockpit and the last passenger location, they are nearly identical at the wingtip after the initial difference. This can be seen especially well in Figures 10 and 11, where the flexible part of the response is much more dominant than the rigid body part. Possible causes of the stated differences are the extent to which the modes influence the acceleration at the discrete points (see the discussion of the Bode plots in the next section) and the inherently different modeling and simulation qualities of CFD and AVL. Furthermore, the CFD modeling options can lead to variances in the results. For example, different turbulence models and meshes lead to pitch angles under trimmed conditions that are up to $0.1\,^{\circ}$ different from each other. Despite the still existing differences, the correction using CDF data shows a significant improvement over the model based solely on AVL data. This can be seen in the Figures 12 and 13 in the Appendix. They show the angle of attack response due to a 0.5 Hz elevator doublet and the acceleration in z-direction at the position of the last passenger after a 10 Hz elevator doublet.

4.2 Frequency Domain Comparison

For a comparison in the frequency domain, Bode plots and the poles of transfer functions (TF) from the elevator deflection to the acceleration in the z-direction at discrete points on the aircraft structure and to the pitch rate at the CG are analyzed and compared. The transfer functions and Bode plots of the non-linear ModSiG model can be easily obtained by linearizing the model. To obtain frequency domain information from the CFD simulation, transfer functions are identified from the available input/output data.

For identification, the function $tfest$ from Matlab [33] is used. Based on the input and output data provided in the time domain, a transfer function is computed that represents the model used to produce the output data. The initial parameter values are determined using the Instrument Variable method. After initialization, the parameters are then updated using non-linear least-squares search methods, which aim to minimize the weighted prediction error norm. A combination of the line search algorithms, *Subspace Gauss-Newton least-squares search*, *Adaptive subspace Gauss-Newton search*, *Levenberg-Marquardt least squares search* and *Steepest descent least-squares search* is tried in sequence at each iteration. The first descent direction leading to a reduction in estimation cost is used [34].

The available data consists of three sets, where the input is the elevator deflection (0.5 Hz or 3 Hz or 10 Hz doublet) and the output data is the local acceleration at three different points: 1. cockpit (CP), 2. position of the last passenger (LPAX) and 3. right wing tip (RWT) and, the pitch rate at the CG. With this data, different transfer functions with various numbers of poles and zeros are identified. For each, the fit to the input/output data used to identify the function and to the other two data sets (the same discrete point, but different input frequency) is calculated with the help of the normalized root mean square error (see Eq. 13). The transfer functions ultimately selected from the generated sets of TFs possess a combination of very high fits and a Bode plot that is similar to the Bode plots of the linearized ModSiG model. The following Table 4 lists the number of poles and zeros and the fits for the selected transfer functions.

Table 4: Parameters of transfer functions identified from CFD data

transfer function	$TF_{\delta_e a_z CP}$	$TF_{\delta_e a_z LPAX}$	$TF_{\delta_e a_z RWT}$	$TF_{\delta_e q CG}$
number of poles $\&$ zeros	$19\,\&\,18$	$21\,\&\,20$	$22\,\&\,21$	$10\,\&\,9$
fit with 0.5 Hz doublet sim. data $[\%]$	95.17	94.03	93.7	93.11
fit with 3 Hz doublet sim. data $[\%]$	99.57	98.38	99.57	99.65
fit with 10 Hz doublet sim. data $[\%]$	98.69	97.19	91.10	95.62
average fit $[\%]$	97.8	96.53	94.79	96.12

The rigid body response is more and the contribution of the flexible dynamics is less pronounced at the CG position. Therefore, a lower order transfer function is adequate to approximate the dynamic response. The influence of flexibility is greater at the other points. Therefore, higher order transfer functions are needed to approximate the system there. The number of poles and zeros of these functions is similar; the small differences are no indicator that for one point more flexible contributions are present. Despite the different excitation frequencies, it is possible to identify models that represent the CFD data with a very high average fit between $93.11\,\%$ and $99.65\,\%$. In the Appendix, in Figures 9, 10 and 11, the time domain responses of these transfer functions, the CFD data and the non-linear ModSiG model data are compared. The corresponding Bode plots are shown in Fig. 8.

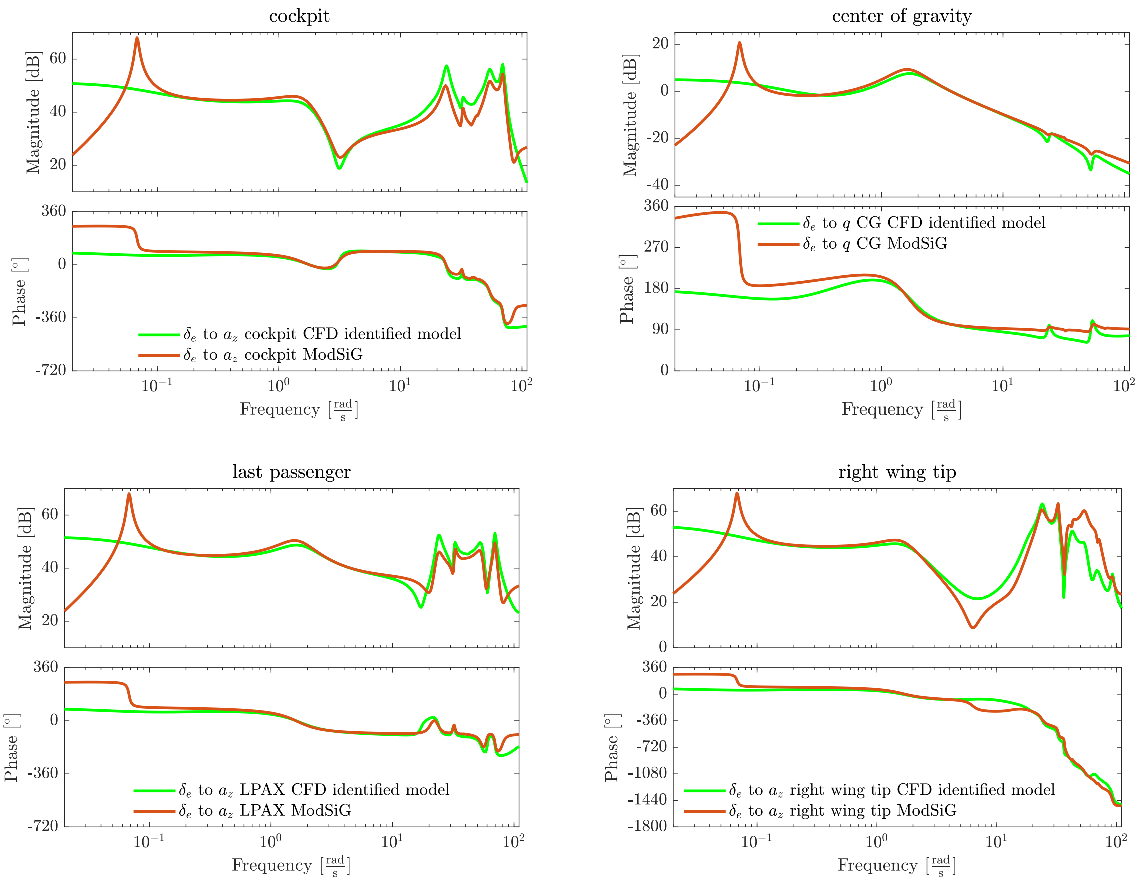

Figure 8: Bode diagrams of the four identified transfer functions from the elevator to a discrete point on the structure

There, almost every peak present in the Bode plot of the linearized ModSiG model is also present in the plot of the identified CFD model. In the frequency range from around $0.1\,\frac{\text{rad}}{\text{s}}$ to around $95\,\frac{\text{rad}}{\text{s}}$, a very good agreement can be observed in the magnitude and frequency of the peaks. This is especially true for the region around $1.75\,\frac{\text{rad}}{\text{s}}$, where the peak that belongs to the short period is, and for the region around $20\,\frac{\text{rad}}{\text{s}}$ to $90\,\frac{\text{rad}}{\text{s}}$, where the elastic modes are visible. The Phugoid mode at around $0.07\,\frac{\text{rad}}{\text{s}}$ is not present in the identified CFD transfer functions. In general, the magnitude of the peaks of the non-linear ModSiG model is slightly higher in the region of the short period and lower in the frequency range of the elastic modes. This is consistent with the fact that, in the time domain, the response of the ModSiG model in the CG is greater (see Fig. 7) and the amplitude of the oscillations of the local accelerations is lower (see Figures 9, 10 and 11) than the CFD data output. In the Bode plot of the wingtip transfer

function, the magnitude of the ModSiG model response is greater than that of the CFD model in the frequency range from around $40\,\frac{\mathrm{rad}}{\mathrm{s}}$ to around $90\,\frac{\mathrm{rad}}{\mathrm{s}}$. Consequently, modes which are present in this frequency range cause greater accelerations in the non-linear ModSiG model simulation. This is consistent with the fact that, in the time domain, it initially reacts with oscillations with higher frequency and amplitude after elevator deflections.
In addition to the visual comparison of the Bode plots, the frequencies of the transfer function poles can be related to the corresponding frequencies of the modes of the linearized ModSiG model (see Table 8 in the Appendix)[1]. The identified modes are collected in Table 5.

Table 5: Mode identification and relation between linearized ModSiG and identified CFD model

CFD identified transfer function poles [$\frac{\mathrm{rad}}{\mathrm{s}}$]	ModSiG transfer function poles [$\frac{\mathrm{rad}}{\mathrm{s}}$]	relative difference [%]	related mode
center of gravity			
1.74	1.65	5.16	short period
18.55	18.95	2.13	1
24.02	25.22	4.78	4
54.21	53.98	0.43	13
cockpit			
1.75	1.65	6.2	short period
18.7	18.95	1.33	1
23.96	25.22	5.02	4
32.28	32.53	0.79	6
42.8	43.72	2.11	11
54.29	53.98	0.68	13
69.59	68.02	2.31	16
73.37	69.8	5.11	18
last passenger			
1.74	1.65	5.6	short period
18.67	18.95	1.53	1
23.95	25.22	5.06	4
32.28	32.53	0.79	6
43.11	43.72	1.38	11
54.29	53.98	0.57	13
69.75	69.8	0.07	18
right wing tip			
1.77	1.65	7.56	short period
19.55	18.96	3.16	1
24.15	25.22	4.27	4
32.31	32.53	0.7	6
37.31	37.51	0.55	7
42.73	43.72	2.26	11
54.2	53.98	0.42	13
65.89	68.02	3.14	16
92.27	91.75	0.57	20

The pole frequencies and the relative difference between the pole frequencies of the transfer

[1]The frequencies of these modes differ from those of the structural NASTRAN model (see Table 7 in the Appendix), since they are frequencies of the aeroelastic modes, i.e. under action of aerodynamics.

functions derived from CFD data compared to those of the linearized ModSiG model are also presented. It can be clearly seen that the transfer functions identified from the CFD data do not accurately represent the complete rigid body dynamics, since the phugoid mode is not present. This is because the doublet inputs do not excite the phugoid mode since their frequency is too high. The frequency of the short period matches quite well (relative error: $5.16\,\% - 7.56\,\%$), but it can be seen that it is always slightly higher in the CFD simulation. The motion of the aircraft in the CG due to the selected inputs seems to be mainly influenced by the short period and not much by the flexibility. Its influence can be seen much better at the other points. There, more poles/flexible modes are present. The difference in frequency of the poles is, with a few exceptions, usually very small (below $5\,\%$).
Similar modes can be identified with the help of the cockpit, the last passenger and the wing tip transfer function. This indicates that the modes that appear in every transfer function are the ones that are primarily present in the longitudinal motion. This assumption can be confirmed by looking at the eigenvectors of the modes. The least amount of modes is identified with the center of gravity transfer function, which is consistent with the expectation that structural flexibility has a lower influence at this location. The presented method is unable to identify all 20 modes of the full order model due to a number of reasons: Firstly, the frequencies obtained this way depend on the accuracy of the identified transfer functions. Secondly, Depending on which discrete point on the structure is excited, different modes can be identified. Third, the input signals are elevator doublets, which may excite only selected modes. However, for the excitation provided, the most important dynamics of the longitudinal motion are well captured by the ModSiG model.

4.3 Computation Time Comparison

Lastly, the difference in computation time is shown in Table 6. There, the computational effort/time required for a five second non-linear simulation of an elevator doublet input (like in Fig. 7) with a sample time of $1000\,\mathrm{Hz}$ is presented. It can be observed that the non-linear ModSiG model is able to compute the results at a fraction of the time needed by the CFD simulation. For the non-linear model simulation, an Intel-Core i7-8700 CPU with 6 cores is used. The CFD simulations are performed on DLR's high performance cluster CARO using 4 computing nodes with 128 cores each. However, the time scales with the number of nodes available on the computing system. Also, the flow conditions influence the computational costs while changing the convergency behavior of the CFD-solver and the required number of iterations.

Table 6: Computational cost between non-linear ModSiG model and CFD simulation

Simulation time	ModSiG Computation time	CFD Computation time
5 s	$\approx 105 - 110$ s	$\approx 55 - 67$ h

5 CONCLUSION

This paper describes a low-order modeling technique based on unsteady aerodynamics strip theory and corrections for transonic effects to obtain the non-linear model of a flexible aircraft with high-aspect ratio wings. It uses the mean axes approach to inertially decouple the equations of the flight dynamics and structural dynamics. The only coupling occurs via the generalized forces and the external aerodynamic forces and moments, which are calculated using the quasi-steady and unsteady incremental aerodynamics approach. The necessary structural parameters, such as, for instance, the eigenvectors and eigenvalues of the structural nodes, are calculated with the help of NASTRAN. The required aerodynamic parameters, like the aerodynamic sta-

bility derivatives, are obtained with AVL and corrected by CFD static analyzes to account for transonic aerodynamics. Neither of these processes is time consuming, so that the generation of new models or model variants (e.g. for new trim points of the flight envelope) can be achieved with little time expenditure.
The process is satisfactorily tested in the project UP Wing to generate a non-linear model of the virtual reference aircraft DLR-F25 at a transonic operating point. For numerical validation, time domain simulations of elevator doublet inputs with different frequencies have been conducted. The results were compared with the simulation results of a more complex model (CFD simulation). They show a good agreement in both the qualitative and quantitative time responses of the states associated with the longitudinal motion in the CG. The response at this point is dominated by the rigid body dynamics, especially by the short period. It displays the same characteristics in both models, with only small differences in frequency and amplitude. Comparisons of local accelerations at discrete points of the structure due to the elevator doublets also show a good agreement between the ModSiG model and the CFD data in the time and frequency domains, especially regarding the flexible dynamics. The magnitude and phase responses are qualitatively and quantitatively similar for the regions of interest, which cover the short period (around $0.26\,\mathrm{Hz}$) and the first 20 modes (from $3\,\mathrm{Hz}$ to $14.6\,\mathrm{Hz}$). The biggest difference in the flexible dynamics between the models occurs shortly after the elevator deflections. At the location of the cockpit and the last passenger, the CFD data shows a greater response, at the location of the wingtip the opposite is true. The minor deviations between the simulations are due to the disregard of the fuselage in the AVL simulation and the inherent differences in the aerodynamic modeling with AVL and CFD. Both factors can be considered with corrections, but not completely compensated for. Dominant modes of the longitudinal motion can be identified from the CFD data and the ModSiG model. The frequency difference between the modes identified with the CFD data and the modes identified with the ModSiG model is very often smaller than $3.5\,\%$ and never greater than $6\,\%$. The non-linear ModSiG model demonstrates a significant computational cost advantage for the simulation of flexible aircraft dynamics, compared to the more complex CFD simulation. Minor compromises in accuracy must be accepted. However, the investigations show that the higher fidelity CFD simulation results can be reproduced well enough and the flexible aircraft dynamics in simulations of the longitudinal motion can be satisfactorily represented. This strengthens the practical utility of the validated model, as conducting numerous qualitative and quantitative accurate simulations in a short time frame enables the use of the model for flying qualities assessment, control system design and virtual flight testing for flexible aircraft.

6 REFERENCES

[1] Bertolin, R., Guimarães Neto, A. B., Barbosa, G. C., et al. (2018). Adaptive output-feedback gain scheduling applied to flexible aircraft. In *CD-ROM Proceedings of 31st Congress of the International Council of the Aeronautical Sciences (ICAS)*. Belo Horizonte.

[2] Gonzalez, P. J. r., Pereira, M. F. V., Silvestre, F. J., et al. (2019). Very flexible aircraft control based on loop-separation and reference governor. In *Proceedings of IFASD International Forum on Aeroelasticity and Structural Dynamics*. Savannah.

[3] Gonzalez, P. J., Silvestre, F. J., Paglione, P., et al. (2016). Linear control of highly flexible aircraft based on loop separation. In *AIAA Atmospheric Flight Mechanics Conference*. p. 3398.

[4] Waszak, M. R. and Schmidt, D. K. (1988). Flight dynamics of aeroelastic vehicles. *AIAA*. doi:10.2514/3.45623.

[5] Hofstee, J., Kier, T., Cerulli, C., et al. (2003). A variable, fully flexible dynamic response tool for special investigations (varloads). In *Proceedings International Forum on Aeroelasticity and Structural Dynamics 2003, June 4-6, 2003*. LIDO-Berichtsjahr=2004,.

[6] Voß, A. (2020). Design and structural optimization of a flying wing of low aspect ratio based on flight loads. Tech. rep., Technische Universität Berlin.

[7] Quesada, A. A. G., Gonzalez, P. J., Barbosa, G. C., et al. (2024). Influence of nonlinear aerodynamic effects on high aspect ratio aircraft model. *International Forum on Aeroelasticity and Structural dynamics (IFASD)*. Last review on 05.02.2025.

[8] Guimarães Neto, A. B., Barbosa, G. C., Paulino, J. A., et al. (2023). Flexible aircraft simulation validation with flight test data. *AIAA Journal*, 61(1), 285–304. doi:10.2514/1.J060960.

[9] Herrmann, B., Theis, J., and Thielecke, F. (2023). Nonlinear system identification of a uav model with distributed aerodynamics and flexible structure. *CEAS Aeronautical Journal*, 14(3), 661–677. doi:10.1007/s13272-023-00674-x.

[10] Su, W. and Cesnik, C. E. S. (2010). Nonlinear aeroelasticity of a very flexible blended-wing-body aircraft. *Journal of Aircraft*, 47(5), 1539–1553. doi:10.2514/1.47317.

[11] Deskos, G., del Carre, A., and Palacios, R. (2020). Assessment of low-altitude atmospheric turbulence models for aircraft aeroelasticity. *Journal of Fluids and Structures*, 95, 102981. ISSN 0889-9746. doi:https://doi.org/10.1016/j.jfluidstructs.2020.102981.

[12] Cardoso Ribeiro, F., Paglione, P., Silva, R., et al. (2012). Aeroflex: A toolbox for studying the flight dynamics of highly flexible airplanes.

[13] Navaratna, P. D. B., Pontillo, A., Rezgui, D., et al. (2024). Wind tunnel investigations of a pitch-free flexible high aspect ratio aircraft model. In *AIAA SCITECH Forum*. doi:10.2514/6.2024-2819.

[14] Drachinsky, A. and Raveh, D. E. (2020). Modal rotations: A modal-based method for large structural deformations of slender bodies. *AIAA Journal*, 58(7), 3159–3173. doi:10.2514/1.J058899.

[15] Wöhler, S., Häßy, J., and Kriewall, V. (2024). Establishing the dlr-f25 as a research baseline aircraft for the short-medium range market in 2035. In *34th Congress of the International Council of the Aeronautical Sciences*.

[16] Feldwisch, J. M. and Bauer, M. (2023). Ultrafloads: A simulation suite and framework for high-fidelity flight loads. *Aerospace*, 10(3).

[17] Senger Franco, R. A., Mickein, W., Quesada, A. G., et al. (2026). Longitudinal load alleviation control and modeling of a high-aspect ratio wing flexible aircraft. In *Proceedings of the 2026 CEAS EuroGNC conference*. Madrid, Spain. doi:10.82124/CEAS-GNC-2026-099.

[18] Silvestre, F. J. (2012). *Methodology for Modelling the Dynamics of Flexible, High-Aspect -Ratio Aircraft in the Time Domain for Aeroservoelastic Investigations*. Mensch und Buch Verlag. ISBN 978-3-86387-316-5.

[19] Silvestre, F. J. and Paglione, P. (2008). Dynamics and control of a flexible aircraft. *AIAA*. doi:10.2514/6.2008-6876.

[20] van Schoor, M. C. and von Flotow, A. H. (1990). Aeroelastic characteristics of a highly flexible aircraft. *Journal of Aircraft*, 27(10), 901–908. doi:10.2514/3.45955.

[21] Silvestre, F. and Luckner, R. (2015). Experimental validation of a flight simulation model for slightly flexible aircraft. *AIAA Journal*, 53, 1–17. doi:10.2514/1.J054023.

[22] GUYAN, R. J. (1965). Reduction of stiffness and mass matrices. *AIAA Journal*, 3(2), 380–380. doi:10.2514/3.2874.

[23] Guimarães Neto, A. B., Silva, R. G. A., Paglione, P., et al. (2016). Formulation of the flight dynamics of flexible aircraft using general body axes. *AIAA Journal*, 54(11), 3516–3534. doi:10.2514/1.J054752.

[24] CAJU (2022). Ultra performance wing. Last review on 08.12.2022.

[25] Cumnuantip, S., Schulze, M., and Krüger, W. R. (2024). Assessment of the aeroelastic stability of high aspect ratio wing aircraft during the preliminary design. In *International Forum on Aeroelasticity and Structural Dynamics, IFASD 2024*.

[26] Streitenberger, K. M. and Feldwisch, J. M. (2025). Cfd-based aeroelastic maneuver and gust loads analysis for a high aspect ratio wing configuration. In *AIAA SCITECH 2025 Forum*. p. 1663. doi:10.2514/6.2025-1663.

[27] Drela, M. and Youngren, H. (2017). Athena vortex lattice. Last review on 05.02.2022.

[28] A. Eberle, B. S. and Reckzeh, D. (2024). Clean aviation ultra-performance wing (up wing). *AIAA Scitech 2024 Forum*. doi:10.2514/6.2024-2109.

[29] Reimer, L., Heinrich, R., Geisbauer, S., et al. (2021). Virtual aircraft technology integration platform: Ingredients for multidisciplinary simulation and virtual flight testing. In *AIAA Scitech 2021 Forum*.

[30] Meinel, M. and Einarsson, G. O. (2010). The flowsimulator framework for massively parallel cfd applications. In *PARA 2010*.

[31] Gerhold, T. (2005). Overview of the hybrid rans code tau. In N. Kroll and J. K. Fassbender (Eds.), *MEGAFLOW - Numerical Flow Simulation for Aircraft Design*. Berlin, Heidelberg: Springer Berlin Heidelberg. ISBN 978-3-540-32382-2, pp. 81–92.

[32] Schwamborn, D., Gerhold, T., and Heinrich, R. (2006). The dlr tau-code: Recent applications in research and industry. In *ECCOMAS CFD 2006 CONFERENCE*. Auf CD.

[33] The MathWorks Inc. tfest - estimate transfer function model. Mathworks.com. Accessed: May 21, 2026. [Online]. Available: https://de.mathworks.com/help/ident/ref/tfest.html.

[34] The MathWorks Inc. tfestOptions - option set for tfest. Mathworks.com. Accessed: May 21, 2026. [Online]. Available: https://de.mathworks.com/help/ident/ref/tfestoptions.html.

ACKNOWLEDGMENTS

The project Ultra Performance Wing (UP Wing, project number: 101101974) is supported by the Clean Aviation Joint Undertaking and its members. Co-Funded by the European Union. Views and opinions expressed are however those of the author(s) only and do not necessarily reflect those of the European Union or Clean Aviation Joint Undertaking. Neither the European Union nor the granting authority can be held responsible for them.

CLEAN AVIATION

Co-funded by the European Union

APPENDIX

The fit of the estimated transfer function with the validation data is calculated with the help of the normalized root mean square error:

$$fit = 100 \cdot \left(1 - \frac{||y - \hat{y}||}{||y - mean(y)||}\right) \tag{13}$$

Here, y is the measured validation data and $\hat{y}$ is the output of the identified model.

Table 7: First 20 eigenvalues of the UP Wing structural model DLR-F25 cruise configuration (MCRUI)

Mode	Frequency f [Hz]	[rad/s]	Description
1	2.43	15.29	1st symmetric wing bending
2	3.14	19.72	1st asymmetric wing bending + engine out-of-plane motion + fuselage in-plane bending
3	3.56	22.37	1st asymmetric wing bending + engine out-of-plane motion + vertical tail in-plane bending
4	3.71	23.31	2nd symmetric wing bending + 1st fuselage out-of-plane bending
5	5.07	31.86	Wing in-plane asymmetric motion + 2nd symmetric wing bending + engine in-plane motion
6	5.19	32.61	Engine out-of-plane motion + 1st wing torsion + fuselage out-of-plane bending
7	5.81	36.51	3rd symmetric wing bending + wing in-plane symmetric motion + engine out-of-plane motion
8	5.84	36.69	2nd asymmetric wing bending + engine out-of-plane motion + horizontal tail asymmetric bending
9	6.51	40.90	3rd symmetric wing bending + wing in-plane symmetric motion + small engine in-plane motion
10	6.73	42.29	Horizontal tail asymmetric bending + small 2nd asymmetric wing bending
11	6.82	42.85	Wing in-plane symmetric motion + 3rd symmetric wing bending
12	7.16	44.99	Engine in-plane motion + horizontal tail asymmetric bending + wing in-plane asymmetric motion
13	8.40	52.78	Horizontal tail symmetric bending
14	8.49	53.34	3rd asymmetric wing bending + horizontal tail asymmetric bending
15	8.99	56.49	Vertical tail bending + horizontal tail asymmetric bending
16	10.78	67.73	4th symmetric wing bending
17	10.83	68.05	4th asymmetric wing bending + vertical tail bending + horizontal tail in-plane bending
18	11.10	69.74	Horizontal tail symmetric bending + 2nd fuselage out-of-plane bending
19	12.67	79.61	Wing in-plane asymmetric motion + horizontal tail on-plane motion
20	14.57	91.55	5th symmetric wing bending + wing in-plane symmetric motion

Table 8: first 20 modes and their frequency of the linearized ModSiG model without Lag states

Mode	Freq. $[\frac{\text{rad}}{\text{s}}]$	Mode	Freq. $[\frac{\text{rad}}{\text{s}}]$	Mode	Freq. $[\frac{\text{rad}}{\text{s}}]$	Mode	Freq. $[\frac{\text{rad}}{\text{s}}]$
1	18.95	6	32.53	11	43.72	16	68.02
2	20.79	7	37.51	12	44.67	17	68.77
3	23.63	8	38.18	13	53.98	18	69.8
4	25.22	9	41.82	14	54.47	19	79.64
5	31.93	10	42.62	15	56.14	20	91.75

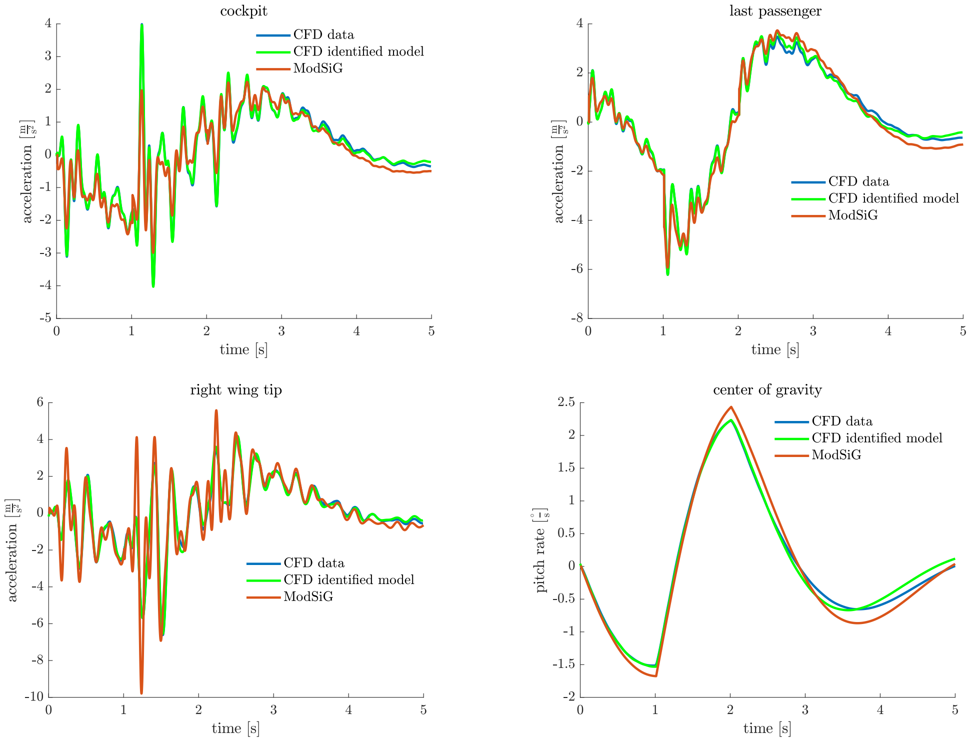

Figure 9: Response of a discrete point on the structure due to a doublet of 0.5 Hz on the elevator calculated by the CFD simulation, the estimated transfer function $TF_{\delta_e a_z}$ ($TF_{\delta_e q}$ for the CG) and the non-linear ModSiG model

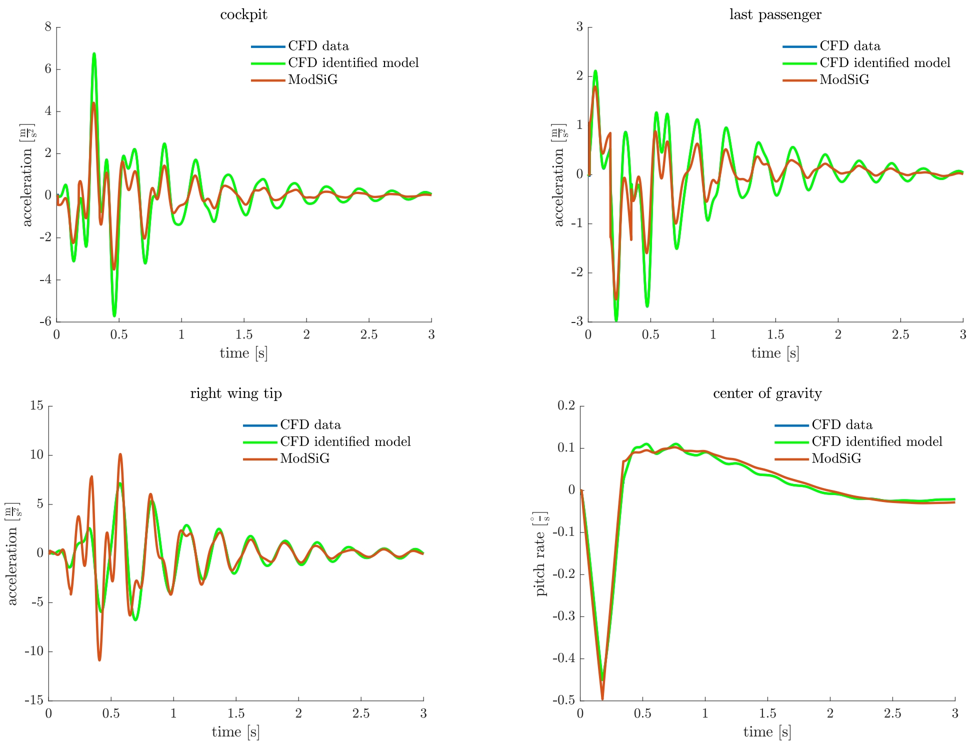

Figure 10: Response of a discrete point on the structure due to a doublet of 3 Hz on the elevator calculated by the CFD simulation, the estimated transfer function $TF_{\delta_e a_z}$ ($TF_{\delta_e q}$ for the CG) and the non-linear ModSiG model

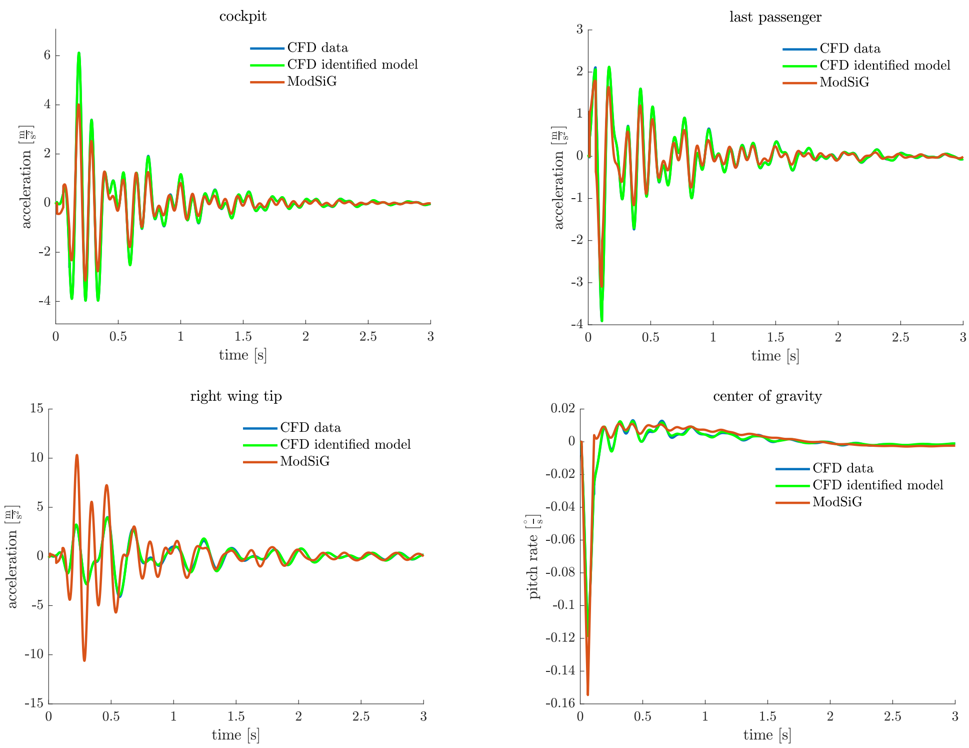

Figure 11: Response of a discrete point on the structure due to a doublet of 10 Hz on the elevator calculated by the CFD simulation, the estimated transfer function $TF_{\delta_e a_z}$ ($TF_{\delta_e q}$ for the CG) and the non-linear ModSiG model

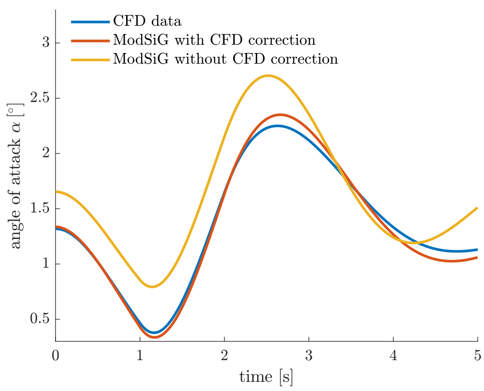

Figure 12: Angle of attack response due to a doublet of 0.5 Hz on the elevator

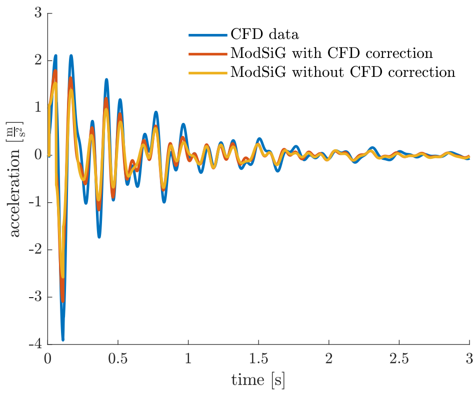

Figure 13: Acceleration in z-direction at the position of the last passenger due to a doublet of 10 Hz on the elevator